Volume 2
Number 6
November 2022
Pages 1239–1570

Environmental Science
Atmospheres

rsc.li/esatmospheres

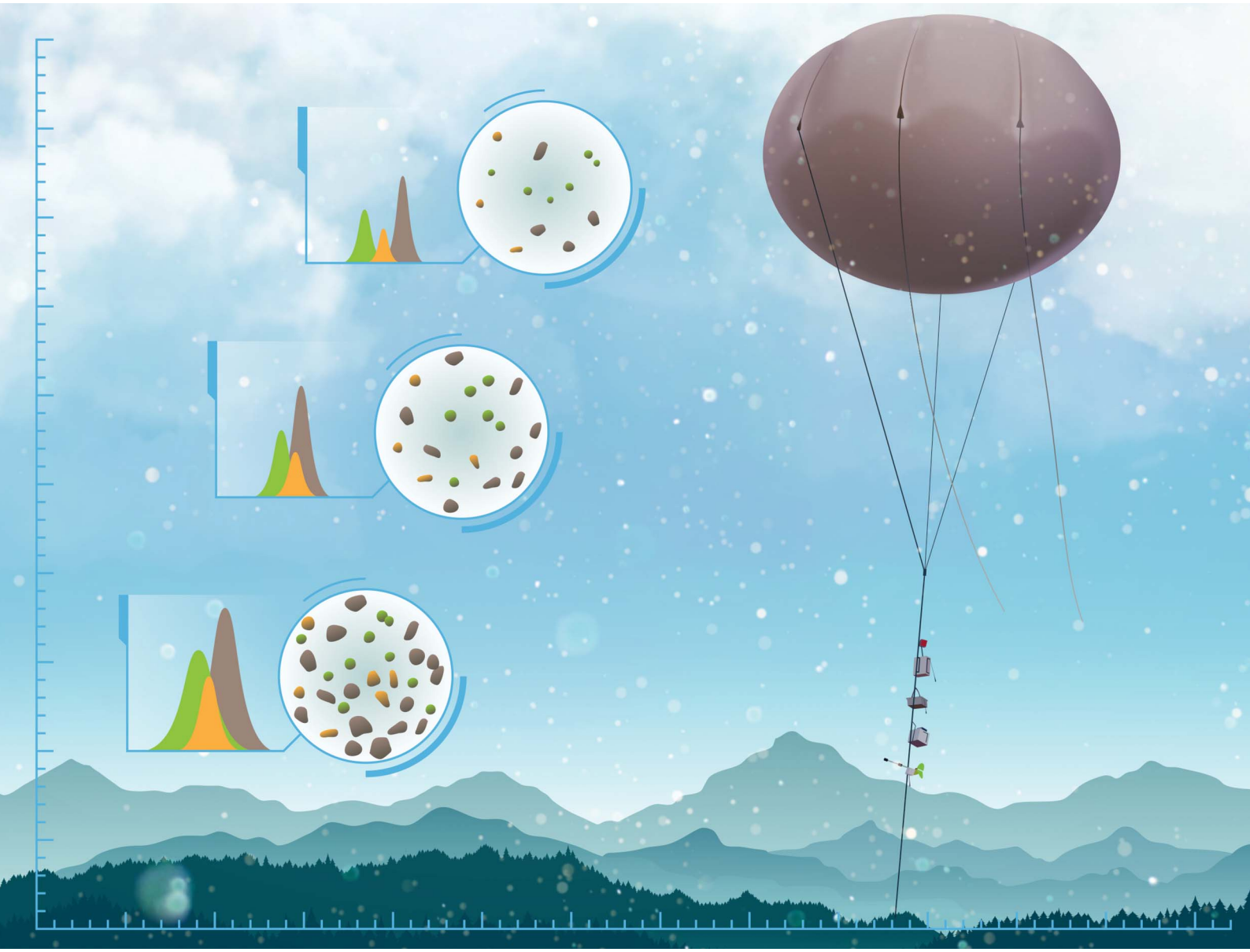

ISSN 2634-3606

ROYAL SOCIETY OF CHEMISTRY

PAPER
Swarup China *et al.*
An automated size and time-resolved aerosol collector platform integrated with environmental sensors to study the vertical profile of aerosols

Environmental Science: Atmospheres

ROYAL SOCIETY OF CHEMISTRY

PAPER

View Article Online
View Journal | View Issue

Cite this: *Environ. Sci.: Atmos.*, 2022, **2**, 1263

An automated size and time-resolved aerosol collector platform integrated with environmental sensors to study the vertical profile of aerosols†

Zezhen Cheng, [a] Andrey Liyu,[a] Darielle Dexheimer,[b] Nurun Nahar Lata, [a] Gourihar Kulkarni,[c] Casey Michael Longbottom,[b] Fan Mei [c] and Swarup China *[a]

Atmospheric particles affect human health, climate, and ecosystems but assessing their impacts is still challenging. Part of that is because of the limited understanding of the size dependence of particle properties and variation of these properties along with the vertical profile under different environmental conditions. Thus, we present a vertical gradient of size-resolved aerosol composition by deploying an automated size and time-resolved aerosol collector (STAC) platform integrated with sensors on the Atmospheric Radiation Measurement's (ARM) tethered balloon system (TBS) at the Southern Great Plains (SGP, Oklahoma) site. Our results highlight variations in atmospheric processing and aerosol sources along the vertical column by showing similar compositions with different size distributions of particles at various altitudes. The platform has been deployed in several other ARM campaigns in Oliktok Point (Alaska), Houston (Texas), and Crested Butte (Colorado). The STAC platform is loaded with an array of 4-stage cascade impactors to collect aerosol particles within different aerodynamic size ranges up to 20 sampling points per flight for various atmospheric research studies, such as the vertical profile of size-resolved aerosol chemical composition and multi-phase chemistry. Time-resolved sampling facilitates the study of the evolution of particles in the atmosphere. The battery-powered, lightweight automated size- and time-resolved sampling system is ideal for unmanned aerial systems (*e.g.*, TBS) and aircraft sampling. The STAC platform is integrated with a temperature and relative humidity sensor and a pressure sensor to monitor ambient conditions, an optical particle counter to measure aerosol size distribution, and a micro-aethalometer to measure the black carbon mass concentration. Experimentally derived 50% cut-off sizes of each stage (stages A to D) for a standard impactor are about 2.3, 0.62, 0.42, and 0.12 μm. The impactor is adaptable to collect smaller particles with an additional replaceable stage E with a 50% cut-off size of 0.07 μm. The STAC platform facilitates simultaneous sampling of aerosols on three different types of substrates for multi-modal offline analysis to probe their physical (*e.g.*, phase state and morphology), chemical (*e.g.*, the elemental composition of individual particles and size-resolved chemical composition), optical (light absorption and scattering), hygroscopic and ice nucleation properties.

Received 30th July 2022
Accepted 12th September 2022

DOI: 10.1039/d2ea00097k

rsc.li/esatmospheres

Environmental significance

Predicting the Earth's radiative balance relies on the vertical distribution of aerosols, which is not well understood partially due to limitations in measurements. Here, we present the vertical distribution of size-resolved aerosol composition over an agricultural site by deploying a newly developed lightweight automated size- and time-resolved aerosol collector (STAC) platform integrated with environmental sensors on unmanned aerial systems (*e.g.*, tethered balloon systems). The compact system is suitable for collecting ambient particles with different size ranges, ambient particle and black carbon concentrations, and meteorological data at different locations and multiple altitudes with high time-resolution. The platform is suitable for various atmospheric research applications, such as to study the vertical profile of size-resolved aerosol chemical composition, multi-phase chemistry, and ice nucleation.

[a]*Environmental Molecular Sciences Laboratory, Pacific Northwest National Laboratory, Richland, Washington 99352, USA. E-mail: swarup.china@pnnl.gov*
[b]*Sandia National Laboratories, Albuquerque, NM, 87185, USA*
[c]*Atmospheric Sciences and Global Change Division, Pacific Northwest National Laboratory, Richland, Washington 99352, USA*

† Electronic supplementary information (ESI) available. See https://doi.org/10.1039/d2ea00097k

1. Introduction

Atmospheric particles can affect climate, human health, and the ecosystem.[1,2] They can directly affect climate by absorbing and scattering solar radiation and indirectly by acting as warm and cold cloud nuclei.[3–8] Moreover, exposure to atmospheric

particles can cause various health problems, such as respiratory, allergic, and cardiovascular diseases.[9–13] Besides these, atmospheric particles can influence rates of photosynthesis and evapotranspiration, alter nutrient inputs through deposition processes, and offer nutrient transport between terrestrial and atmospheric systems.[2]

Understanding atmospheric particles' chemical composition and size distribution is crucial for improving our knowledge of these effects. It has been found that atmospheric particles have complex and diverse chemical compositions and multi-components in nature, including but not limited to carbonaceous particles (*e.g.*, black carbon and organic carbon particles), sea spray aerosols (*e.g.*, sea salt), bioaerosols (*e.g.*, fungi, bacteria, viruses, and pollen), and dust, and their size distributions are also highly variable.[3,14–16] Even more complicated is the vertical profile of atmospheric particles, which might alter particles' properties due to variations in ambient conditions and their being involved in different atmospheric processes (*e.g.*, cloud processes and atmospheric aging processes) at different atmospheric layers.[17–21] Conversely, the vertical profiles of atmospheric particles are also essential for regional and global climate since they have critical impacts on the atmospheric thermal structure, cloud dynamics, regional-to-global circulation systems, lower atmospheric thermodynamic stability, and planetary boundary layer development.[17,22,23] Furthermore, climate models also need a more precise vertical profile of atmospheric particles to reduce the uncertainties of radiative forcing of atmospheric particles related to vertical aerosol dispersion.[24–28] Thus, the chemical composition and size distribution of atmospheric particles as a function of height are critical to understanding the interaction between aerosols and the atmospheric boundary layer.

There were numerous measurements conducted at ground-level sites[29–32] and at high altitudes *via* aircraft measurements[33–37] to investigate the chemical and size distribution of atmospheric particles, but these measurements were usually limited in the number of different altitudes and operationally expensive. Moreover, in some cases, particle concentrations are low for online measurements and some sites are difficult to access. Besides these field measurements, remote sensing, such as the Aerosol Robotic Network (AERONET), has also been used to estimate the particle size distribution and particle types within the total atmospheric column,[38,39] which cannot represent the vertical distribution of particles.

Recently, unmanned systems have been increasingly utilized for atmospheric particle measurement due to the advantages of minimizing environmental research errors, risks, and costs. One example is the tethered balloon system (TBS), which has been deployed in several field campaigns to study aerosol properties.[17,40–46] Along with these different TBSs, the U.S. Department of Energy's (DOE) Atmospheric Radiation Measurement (ARM) program developed a TBS, which has been deployed at several ARM atmospheric observatories such as the North Slope of Alaska (NSA) site and Southern Great Plains (SGP) site.[46–48]

Although the TBS has the advantages mentioned before, the total weight of instruments loaded on it is limited, prohibiting some heavy-weight online instruments. This brings up opportunities for collecting samples using impactors for comprehensive offline measurements. There are several commercial cascade impactors, such as the microorifice uniform deposit impactor (MOUDI, TSI),[49] Sioutas personal cascade impactor sampler (PCIS, SKC Ltd)[50,51] and rotating drum impactor (RDI) sampler[52–54] which provide size-resolved aerosol sample collection. However, the MOUDI is about 11–12 kg and requires a large flow rate pump and high energy support, making it unsuitable for the TBS. Although the PCIS has a much smaller weight than the MOUDI (PCIS is about 0.16 kg), the smallest 50% cut-off of the PCIS is 0.25 μm, making it inefficient in collecting small particles and not providing a time-resolved aerosol sampling. Atmospheric events might change rapidly along the vertical column, underscoring the demand for a high time resolution sampler. Although the RDI sampler can collect size- and time-resolved particles, it is still unsuitable for TBS sampling due to weight and power constraints.

Therefore, the main objective of this study was to study the vertical distribution of aerosol composition by deploying an automated size and time-resolved aerosol collector (STAC) platform integrated with environmental sensors, which is light weight and can be deployed on the ARM's TBS. The STAC platform can be equipped with a maximum of 20 4-stage STAC impactors, allowing us to collect particles in specified size ranges with high time resolution for multi-modal microscopy, spectroscopy, and mass spectrometry platforms to probe particle physical and chemical properties. We aim to enhance the capability of collecting atmospheric particles at multiple altitudes to improve our knowledge of the vertical profile of atmospheric particles.

2. Methods

2.1 Design of the STAC platform

Fig. 1 shows the schematic of the size- and time-resolved aerosol collector (STAC) platform. The STAC platform is a lightweight (39.3 (L) × 22.5 (W) × 14.6 (H) cm, 7.5 kg) automated aerosol particle collector and meteorological condition monitor which has been deployed on the ARM's TBS. It aims to investigate the variation of particle size-resolved physical and chemical properties vertically under different environmental conditions. The STAC platform is powered by a 76 W h, 21.8 V Li-ion battery and utilizes a single-board computer (Model X86 II ULTRA, UDOO) with an Arduino Leonardo and a custom-made circuit board to control solenoid latched valves (model L31012VDC, Humphrey) and a 3 LPM pump (Model B1B-090V12AN-00, Parker Hannifin) for collecting samples on an array of 4-stage STAC impactors, which allows users to program the sample collection time and the number of samples.

The STAC platform is integrated with a temperature and relative humidity sensor (Model SEN0385, DFRobot) and a pressure sensor (Model BMP280, Adafruit Industries) to monitor the meteorological conditions along with sampling, and an inline pressure sensor (Model MPRLS0025PA00001AB, Honeywell) to monitor the pressure in the sampling line as an indicator of the performance of valves and pumps. The changes in flow rates are negligible since pressure fluctuations are

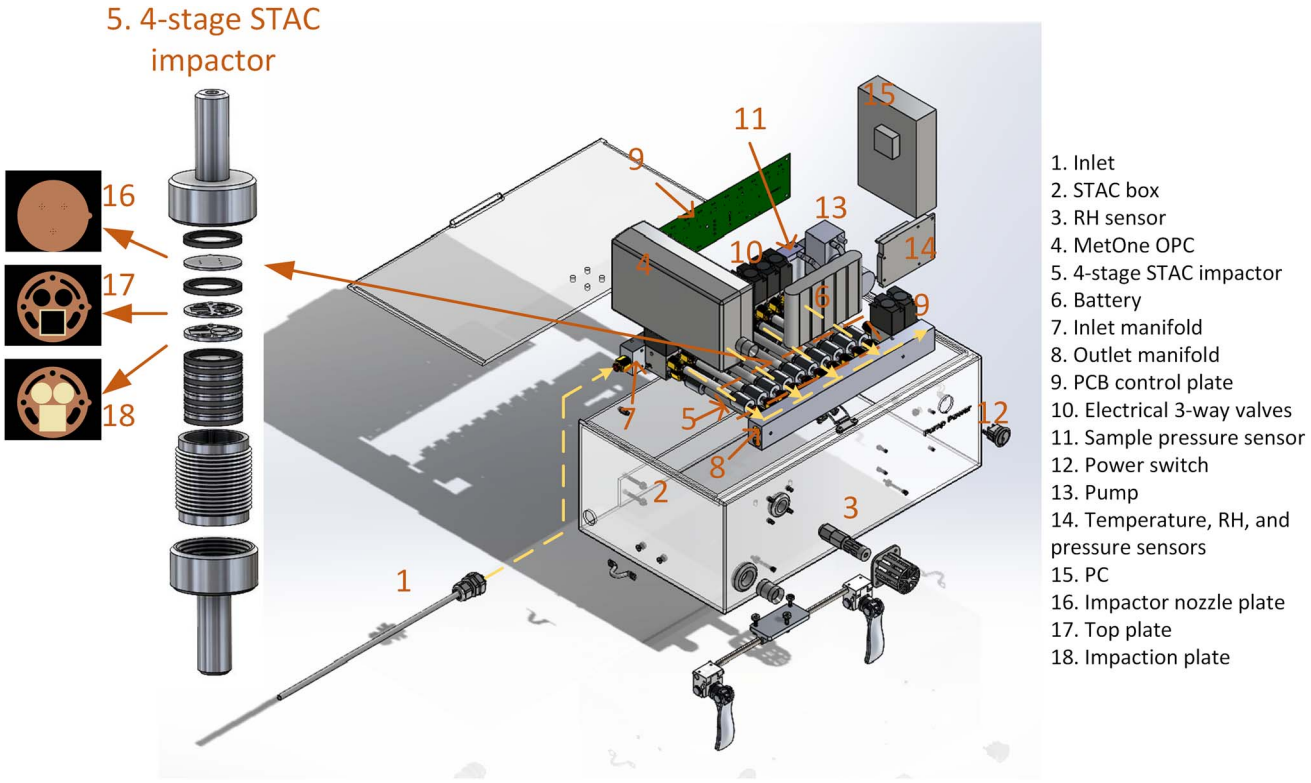

Fig. 1 Schematic showing the major components of a size- and time-resolved aerosol collector (STAC) platform and 4-stage STAC impactor. The numbers indicate[1] Sample inlet,[2] STAC box,[3] RH sensor,[4] MetOne OPC,[5] 4-stage STAC impactor,[6] battery,[7] inlet aluminum manifold,[8] outlet aluminum manifold,[9] printed circuit board (PCB) control plate,[10] electrical 3-way valves,[11] sample pressure sensor,[12] power switch,[13] pump,[14] Temperature and altitude sensors,[15] PC,[16] impactor nozzle plate,[17] top plate, and[18] impaction plate. A micro-aethalometer (microAeth, Model MA200, AethLabs) is attached (not shown here) to the outside bottom of the STAC box. Yellow arrows indicate the direction of the aerosol flow.

within 5% during the flights. All sensors are controlled through the I2C interface from the Arduino Leonardo. A custom software application is written in LabVIEW and works on Windows 10 Pro. Communication between LabVIEW and the Arduino Leonardo is in the LINX library. The STAC platform is also equipped with a portable optical particle counter (OPC, Model 804, MetOne) to measure aerosol size distribution in the 0.3–2.5 μm range. All components of the STAC platform are placed inside a customized 3D-printed box. We also have a micro-aethalometer (microAeth, Model MA200, AethLabs) attached to the outside bottom of the STAC box to measure the light-absorption coefficient of aerosols at 375, 470, 528, 625, and 880 nm wavelengths to investigate the dependence of aerosol light-absorption properties on ambient conditions. The STAC platform is loaded with an array of 4-stage cascade impactors (maximum of 20) to collect particle samples on different substrates (*e.g.*, carbon B-films, carbon lacey, and silicon nitride substrates) for multi-modal offline analysis to probe their physical, chemical, and optical properties. For example, collected samples can be utilized for offline analysis of phase states,[55] phase separations,[56] morphology and mixing states of particles,[57–59] and to evaluate their size-resolved chemical composition.[60] Particles collected on TEM grids can be probed to study hygroscopic behavior,[61,62] and particles collected on

Table 1 Design and operating parameters of the STAC impactor (sampling flow rate: 3LPM)

Stage	Pressure above the impaction plate (cm Hg)	U (cm s^{-1})	D, hole diameter (μm)	Number of holes	$d_{p,50,design}$ (μm)	$d_{p,50,theo}$[a] (μm)	$d_{p,50,exp}$[b] (μm)	Geometric standard deviation (σ_g)
A	741.2	979.10	1041.4 ± 8.3	6	2.5	2.39 (1.84–3.11)	2.27 (1.68–2.89)	4.97
B	730.2	4047.52	512.1 ± 3.0	6	0.6	0.620 (0.449–0.856)	0.615 (0.571–0.651)	1.39
C	718.9	4747.48	386.1 ± 2.5	9	0.45	0.447 (0.317–0.628)	0.421 (0.413–0.429)	1.34
D	703.6	10 610.33	200.6 ± 3.4	15	0.15	0.133 (0.089–0.200)	0.119 (0.117–0.121)	1.53
E	540.6	16 578.64	158.1 ± 3.1	15	0.05	0.057 (0.037–0.090)	0.069 (0.067–0.070)	1.47

[a] The numbers inside brackets represent the range of uncertainties of the theoretically derived 50% cut-off size ($d_{p,50,theo}$) based on the particle densities in the literature. [b] The numbers inside brackets represent the range of uncertainties of the experimentally derived 50% cut-off size ($d_{p,50,exp}$).

silicon nitride substrates can be utilized for ice nucleation studies.[60,63] Furthermore, particles collected on lacey TEM grids will facilitate studies of optical properties (light absorption and scattering) of electron beam-resistant spherical particles using electron energy loss spectroscopy.[64]

2.2 Design of 4-stage STAC impactors

The middle panel of Fig. 1 shows the schematic of a 4-stage STAC impactor, which is a miniaturized cascade impactor. The height of the STAC impactor is ~54.0 mm and the diameter is ~16.5 mm. The total weight of a STAC impactor is ~11.0 g. Each stage includes an impactor nozzle plate with different numbers and sizes of round micro-orifices (see Table 1), an impaction plate to hold substrates, and a top plate to secure the plate (see right panel of Fig. 1). These plates are made of a printed circuit board (PCB) coated with copper. We used micro drills to make the micro-orifices on the impactor nozzle plates. We use a 1 mm wide, 9 mm ID square profile rubber O-ring to seal between the plates. These plates are stacked together in an aluminum cylinder, which includes two caps with a $\frac{1}{4}$ inch inlet and a cylinder body to hold the plates. The design and choice of the material allow us to minimize the weight and avoid particle losses due to electrostatic deposition. The standard setup of a 4-stage STAC impactor includes stages A, B, C, and D. The impactor is adaptable to collect smaller particles with an additional replaceable stage E.

The design of impaction stages was based on Marple and Willeke, 1975, which is well-documented and widely used. The design of impactor stages was based on the desired 50% cut-off particle size ($d_{p,50}$), for which 50% of the particles will be collected on the impaction plate. $d_{p,50}$ can be calculated based on Stokes' number at 50% collection efficiency (St_{50}):

$$St_{50} = \frac{\rho_p d_{p,50}^2 C_c U}{9\mu D} \quad (1)$$

where C_c is the slip correction factor, U is the average jet velocity through the nozzle (cm s^{-1}), D is the impactor's nozzle diameter (μm) (estimated based on the designed value), ρ_p is the particle density, and μ is the dynamic viscosity of air (0.0182 g cm^{-1} s^{-1}). We assume that ρ_p is equals to 1.6 g cm^{-3} to represent laboratory-generated and ambient particle density.[66–74] The C_c is given by the equation:[65]

$$C_c = 1 + \frac{0.163}{Pd_p} + \frac{0.0549}{Pd_p}\exp(-6.66Pd_p) \quad (2)$$

where P is the air pressure at the impaction plate and d_p is the particle diameter (μm). For round-nozzle impactors, the St_{50} is 0.7.[75] Thus, based on our designed $d_{p,50}$ ($d_{p,50,design}$) of each stage (2.5, 0.6, 0.45, 0.15, and 0.06 μm, respectively), we designed the size and number of nozzles of each stage's impactor nozzle plate.

2.3 Laboratory evaluation of collection efficiency of each impactor stage

To evaluate the performance of the STAC impactor, we performed experiments with laboratory-generated aerosols. First, we measured the hole size of impactor nozzle plates (D) using an environmental scanning electron microscope (ESEM, Quanta 3D, Thermo Fisher) equipped with an FEI Quanta digital field emission gun, operated at 20 kV and 480 pA. We used a temperature- and pressure-compensated mass flowmeter (model 5200-2, TSI, Inc.) to measure the pressure drop of each impactor nozzle plate (ΔP_x, where x is equal to the stage number (A, B, C, D, and E)) and impaction plate ($\Delta P_{impaction}$), and used these values to estimate the pressure at each impaction plate ($P_x = P_{ambient} - \sum \Delta P_x - a\Delta P_{impaction}$, where a is equal to the number of stages before stage x (0–3)). P_E is calculated by using the set of stages A, B, C, and E. Different sets of stages might change the pressure on the impaction plates, thus altering the 50% cut-off size. Based on measured parameters (P_x, U, and D) and assumed particle density ($\rho_p = 1.6$ g cm^{-3}), we used eqn (1) and (2) to calculate each stage's theoretical 50% cut-off size ($d_{p,50,theo}$) and listed it in Table 1. However, several studies have reported that particle density might vary between 1 and 2.5 g cm^{-3}.[67,69,72,74,76–78] To account for the ambient particle density variation, we also include $d_{p,50,theo}$ calculated by using ρ_p equal to 1 and 2.5 g cm^{-3} as uncertainties in Table 1.

To evaluate the performance of the impactor, we calculated the collection efficiency (η) of each stage using:

$$\eta = \frac{n_{d_p,\,\text{before}} - n_{d_p,\,\text{after}}}{n_{d_p,\,\text{before}}} \times 100\% \quad (3)$$

where $n_{d_p,\,\text{before}}$ and $n_{d_p,\,\text{after}}$ are the particle number concentrations at d_p before and after the impactor stage. $n_{d_p,\,\text{before}}$ is measured as the total particle concentration before an impactor and $n_{d_p,\,\text{after}}$ is measured as the total particle concentration after an impactor with the impaction plate. We use ammonium sulfate (AMS) particles, laboratory-generated polystyrene latex microspheres (PSL, sizes are 0.803 ± 0.014, 1.592 ± 0.016, 2.994 ± 0.031, and 6.007 ± 0.040 μm), and deionized (DI) water droplets to determine the collection efficiency of particles. AMS particles and DI water droplets were generated by atomizing 500 mL of ~10 g L^{-1} AMS solution and 400 mL DI water, respectively, with a nitrogen flow at 3 LPM using an aerosol generator (model 3076, TSI, Inc.), and PSL particles were generated by nebulizing ~4 mL of ~0.01 vol% PSL solution with 2 LPM nitrogen using a medical nebulizer (8900-7-50, Salter Labs, Inc.). We conditioned AMS and PSL particles in a diffusion dryer (model 306 200, TSI, Inc.) to reach a relative humidity below 15%. AMS solution was prepared by dissolving ~4 g AMS (CAS number: 7783-20-2, Sigma Aldrich) in ~0.4 L DI water. PSL solution was prepared by diluting concentrated PSL solution (Part numbers: AP3800A, AP4016A, AP4016A, and AP4206A, respectively, Applied Physics, Inc.) with DI water. We used a scanning mobility particle sizer (SMPS, TSI, Inc.) to measure the number size distribution within the size range of 0.01–1 μm. The SMPS includes an electrostatic classifier (Model 3082, TSI, Inc.) coupled with a long differential mobility analyzer (DMA, Model 3081A, TSI, Inc.) and a versatile water-based condensation particle counter (WCPC, model 3789, TSI, Inc.). To calculate the collection efficiency of particles larger than 1 μm, we used an optical particle counter (OPC, Model 804, Met One Instruments, Inc.) to measure the concentration of the particles

before and after stage A in size ranges of 0.7–1, 1.0–2.5, 2.5–5.0, and 5.0–10.0 μm. The OPC was calibrated before the experiment, and the uncertainty of each size range was within 10%. This uncertainty has been accounted for in the measurement uncertainties. This study only used AMS particles for SMPS measurements and PSL particles and DI water droplets for OPC measurements.

Moreover, we collected dry Suwannee River fulvic acid (SRFA, 1S101F, International Humic Substance Society) particles and Arizona test dust (ATD, ISO 12103-1, A1 ULTRAFINE TEST DUST, Powder Technology Inc.) particles with a STAC impactor to evaluate the size range of particles on each impactor stage. Dry SRFA particles were generated using a medical nebulizer (model 8900-7-50, Salter Labs, Inc.) by nebulizing 3 mL of 500 ppm SRFA DI water solution with a nitrogen flow at 2 LPM and then drying the stream with the same diffusion dryer. Dry ATD particles were generated using a customized dry particle disperser by blowing 3 mg ATD with a nitrogen flow at 1 LPM. We also added an additional nitrogen flow to SRFA and ATD sample flows to make up the total flow rate needed for the STAC impactor. Dry SRFA and ATD particles were collected on carbon Type-B TEM grids (Ted Pella Inc) loaded on the impaction plate of each stage and then used computer-controlled scanning electron microscopy with energy-dispersive X-ray spectroscopy (CCSEM-EDX) to probe their area equivalent diameter.[79,80] CCSEM-EDX utilizes an ESEM (Quanta 3D, Thermo Fisher) equipped with an FEI Quanta digital field emission gun, operated at 20 kV and 480 pA, to retrieve individual particles' shape, morphology, and projected size (area equivalent diameter) based on their ESEM images. The CCSEM-EDX is equipped with an EDX spectrometer (EDAX, Inc.) to probe the spectra of individual particles. SRFA has advantages such as dry SRFA particles are spherical and stable under an electrical beam and have a wide size distribution (from <100 nm to >5 μm).[55,81,82]

2.4 Field deployment of the STAC platform on a tethered balloon system

We deployed the STAC platform *via* the ARM's TBS to collect ambient particle samples and meteorological data at the SGP atmospheric observatory (DOE's ARM mega-site), located near Lamont, in north-central Oklahoma, on February 14th, 2022. Ambient particles were collected on multiple substrates (TEM B-film grids, lacey grids, and silicon nitride substrates) loaded on 4-stage STAC impactors. The STAC platform is also equipped with an OPC and a micro-Aeth. During each TBS flight, the STAC platform was attached to the TBS along with one condensation particle counter (CPC, model 3007, TSI) and one printed optical particle spectrometer (POPS, Handix Scientific) to measure the particle concentration and size distribution, one iMet radiosonde, and one wind speed and direction sensor to monitor meteorological conditions. The TBS was launched at 18:25 (UTC) and grounded at 21:38 (UTC). Sample collection conditions are illustrated in Table S1.† During this flight, we collected 5 STAC impactors (IM1–IM5). IM1 was collected when the STAC platform was loitering at ~200 m above ground level (AGL), IM2 was collected when the STAC platform was ascending from ~200 m AGL to ~400 m AGL, IM3 was collected when the STAC was loitering at ~400 m AGL, IM4 was collected when the STAC platform was ascending from ~400 m AGL to ~700 m AGL, and IM5 was collected when the STAC platform was ascending from ~700 m AGL to ~850 AGL. Each impactor sample was collected for 30 min. Under these sampling conditions, around 10^5 particles per STAC impactor are deposited. This particle loading is suitable for multi-modal offline analyses. Typically, similar particle concentrations are needed for chemical composition, optical properties, and ice nucleation measurements. Lower particle loadings are needed for relative humidity-dependent phase state and hygroscopicity measurements as particles will grow and coalesce after water uptake. We select an area away from the center impaction point for these experiments, where particle loadings are lower.

In this study, we focus only on the vertical distribution of aerosol composition using single particle analysis *via* CCSEM-EDX and scanning transmission X-ray microscopy with near-edge X-ray absorption fine structure spectroscopy (STXM-NEXAFS). We performed CCSEM-EDX analysis on stage C and D samples to characterize the morphology and quantify the relative element percentage of 15 elements (C, N, O, Na, Mg, Al, Si, P, S, Cl, K, Ca, Mn, Fe, and Zn) of individual particles in field-collected samples. Due to the lack of coarse mode particle concentrations during this case study, stage A and B particle loadings were poor. We focused on stage C and D samples because of sufficient loadings for CCSEM-EDX analysis. Based on their relative elemental percentage, we classified each particle as carbonaceous, sulfate, sodium-rich (Na-rich), sodium-rich with sulfate (Na-rich/sulfate), dust, silicon with sulfate (Si + S), potassium with sulfate (K + S), and others using previously defined parameters.[60]

Moreover, we also used STXM-NEXAFS at beamline 5.3.2.2 of the Advanced Light Source (ALS) at the Lawrence Berkley National Laboratory to probe the carbon functional groups and mixing state of organic (OC), inorganic (IN), and elemental carbon (EC).[83–88] STXM uses a monochromatic soft X-ray beam generated from a synchrotron light source and a zone plate with 25 nm outer zones to focus on spotting size. The transmitted intensity of X-rays at each pixel in STXM images is recorded by raster scanning the sample under fixed beam energies.[83]

3. Results and discussion

3.1 Measurements of pressure drop at each stage and a theoretical 50% cut-off diameter

Table 1 summarizes the STAC impactor's design and operating parameters for the 3 LPM sampling flow rate. As shown in Table 1, the tolerance of the nozzle hole diameter is less than 2% and increases with the decrease in the hole diameter. This is expected due to the mechanical vibration when using a smaller drill. The pressure above the impaction plates decreases gradually from stage A to stage D. However, the pressure above the stage E impaction plates decreases sharply due to the smaller nozzle size. The theoretical 50% cut-off sizes ($d_{p,50,theo}$) derived based on the measured pressure above the impaction plate and nozzle size for stage A to stage E are about −4%, 3%, 12%,

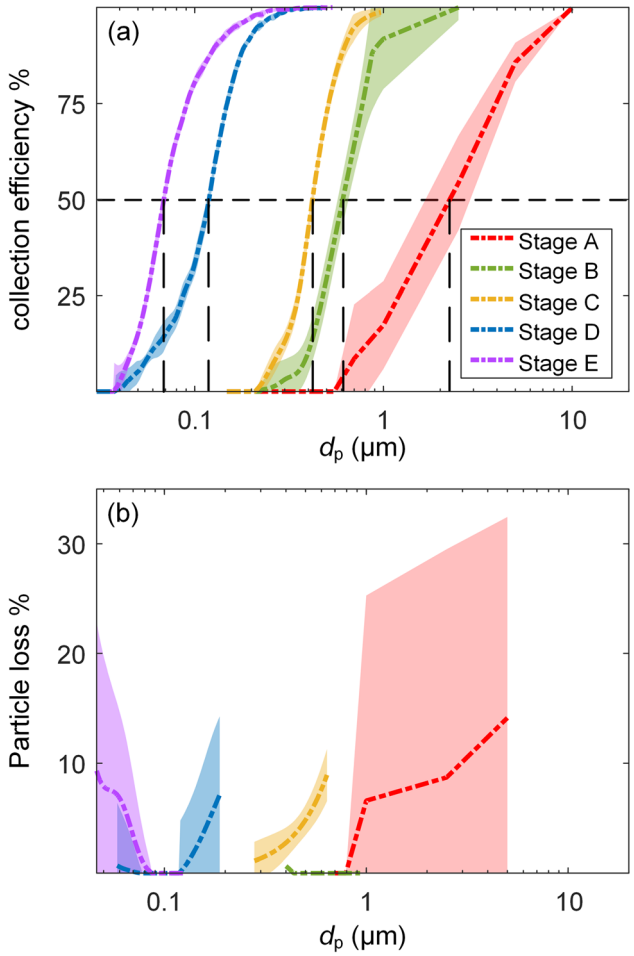

Fig. 2 (a) Particle collection efficiency at each stage as a function of particle diameter (d_p). (b) Particle loss at each stage as a function of d_p. The shaded areas represent uncertainties in collection efficiency.

−11%, and 15% different from the designed 50% cut-off size ($d_{p,50,design}$), validating our design. The increase in the difference between $d_{p,50,theo}$ and $d_{p,50,design}$ might contribute to the increased variance of nozzle diameter from stage A to E.

3.2 Laboratory evaluation of impactor stages

3.2.1. Collection efficiency of laboratory-generated particles. Laboratory-generated particle collection efficiency for each stage as a function of particle diameter (d_p) is plotted in Fig. 2(a). The experimentally derived 50% cut-off particle sizes ($d_{p,50,exp}$) and uncertainty size ranges of $d_{p,50,exp}$ for each stage are 2.27 (1.68–2.89), 0.615 (0.571–0.651), 0.421 (0.413–0.429), 0.119 (0.117–0.121), and 0.069 (0.067–0.070) μm, respectively (see Table 1). The collection efficiency for stage A retrieved from the OPC is the average of DI water droplets and PSL particles, and we used logarithmic interpolation to retrieve the diameter at a certain collection efficiency. To evaluate the performance of each stage of the STAC impactor, we compared the $d_{p,50,exp}$ with $d_{p,50,theo}$. As shown in Table 1, $d_{p,50,exp}$ values for each stage are very close to $d_{p,50,theo}$, and the differences between $d_{p,50,exp}$ and $d_{p,50,theo}$ are about 5.4%, 0.88%, 5.8%, 10.7%, and −20.3%, respectively. The difference between $d_{p,50,exp}$ and $d_{p,50,theo}$ increases from stage B to E, which might be due to the increased variance of nozzle diameters and pressure drop across the impactor nozzle plates. Moreover, the difference between stage A $d_{p,50,exp}$ and $d_{p,50,design}$ and $d_{p,50,theo}$ might be partially due to the wide width of the size bin of the OPC, which measures the total particle count of particles with d_p between 1 μm and 2.5 μm. Moreover, only stage E has a 50% cut-off size larger than the theoretical value due to the more significant particle loss of the stage E impactor nozzle plate caused by the smaller nozzle hole size (see Fig. 2(b)). For stages B and C, the uncertainty in $d_{p,50,exp}$ increases with the particle size due to the decrease in particle concentrations for particles larger than 0.7 μm.

Particle loss in each stage within the size range of 10% and 90% collection efficiency is evaluated by removing the impaction plate and measuring the AMS particles, PSL particles, and DI water droplet concentration before and after the STAC impactor using the SMPS and OPC. As shown in Fig. 2(b), the curves of particle loss as a function of particle diameter for each stage have a U-shape due to increasing diffusion loss with the decrease in particle size and increased gravitational and inertial deposition loss with the increase in particle size. Overall, for each stage, the particle loss is significantly lower than the collection efficiency in the collection particle size range of stages B to E (less than 10%). However, particle loss can increase to more than 14% for stage A when particles are larger than 5 μm. This might be because of increasing static electricity loss caused by rubber O-rings inside the impactor and deposition loss of larger particles.

The precision in particle separation characteristics of each impactor stage is represented by the sharpness of the collection efficiency curve of that stage, which can be quantified in terms of the geometric standard deviation (σ_g, $\sigma_g = (d_{p,84\%}/d_{p,16\%})$, where $d_{p,84\%}$ and $d_{p,16\%}$ are the particle diameters corresponding to 84% and 16% collection efficiency, respectively).[65] The experimentally derived σ_g values for each stage are listed in Table 1. Theoretically, lower σ_g values indicate better particle separation at an impactor stage. As shown in Table 1, the σ_g values of stages B to E are approximately 1.24–1.53, indicating reasonably sharp aerodynamic particle separation characteristics of each stage. However, σ_g for stage A is ∼4.97, which is significantly larger than that of other stages. The wider size bin of the OPC might respond to this large σ_g.

3.2.2. Laboratory evaluation of the collected particle size range at each stage. Particle size distributions and representative ESEM images of dry SRFA particles and ATD particles at each stage are shown in Fig. 3. As shown in Fig. 3(a–e), SRFA particles collected on stages A, B, C, D, and E have size ranges of ∼0.36–5.7 μm, ∼0.23–2.8 μm, ∼0.14–1.4 μm, ∼0.071–1.8 μm, and ∼0.045–0.71 μm, respectively. The size modes for stages A, B, C, D, and E are ∼1.4 μm, ∼0.90, ∼0.43, ∼0.38, and ∼0.11 μm, respectively. The ATD particles collected on stages A to D have size ranges of ∼0.45–7.1 μm, ∼0.23–2.5 μm, ∼0.18–1.8 μm, and ∼0.11–1.8 μm, with size modes at ∼1.4, 0.75, 0.45, and 0.40 μm, respectively (Fig. 3(f–i)), agrees well with the experimentally estimated collection efficiency. Sub-micron size particles (smaller than 1 μm) were collected at stage A due to the inertial deposition of small particles. We have observed ∼14.1% of ATD

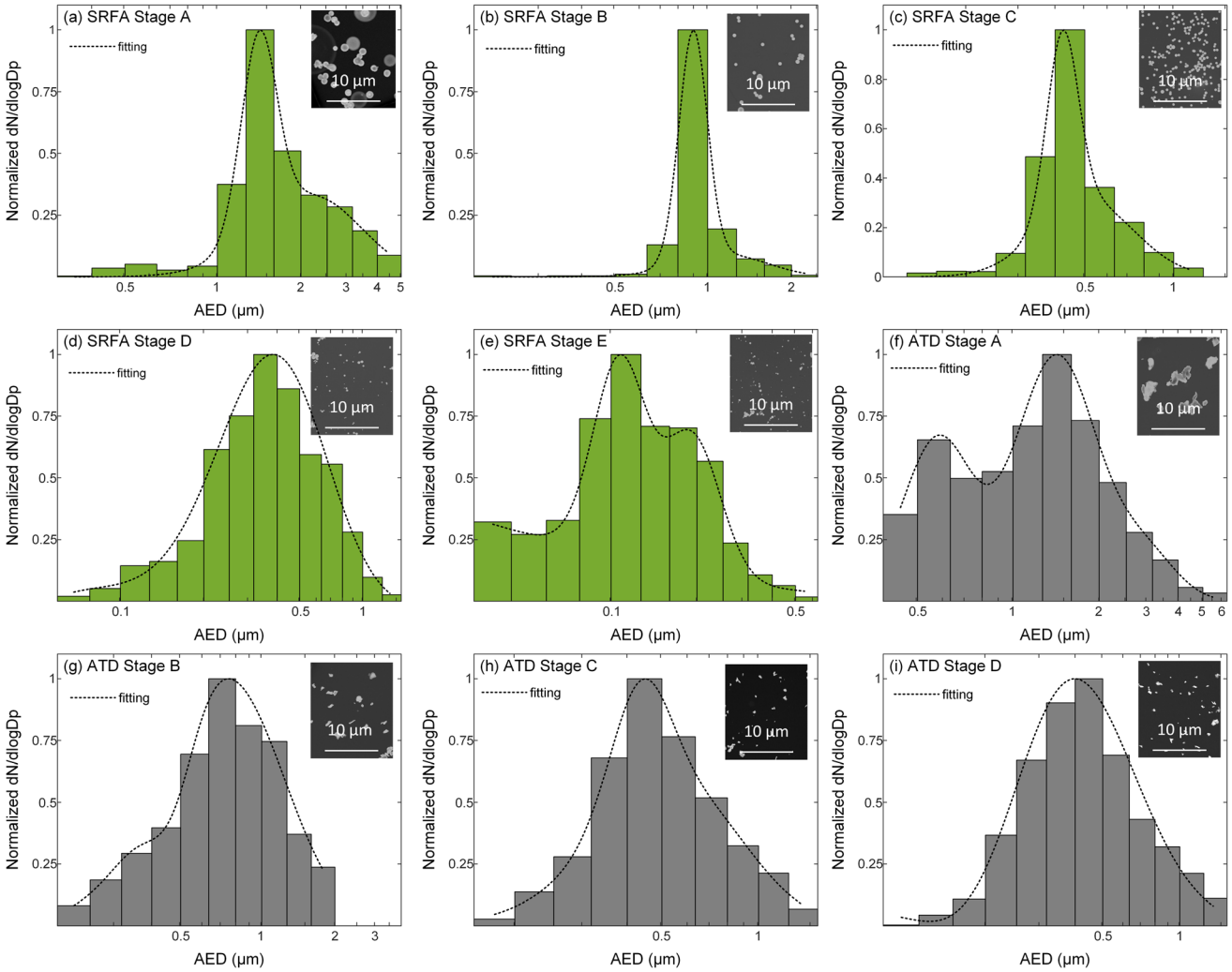

Fig. 3 CCSEM-EDX measured particle size distribution of SRFA particles collected on stage A to E (a to e) and ATD particles collected on stage A to D (f to i). The insets are representative ESEM images of particles at each stage. AED stands for area equivalent diameter. The black dashed lines represent Gaussian fitting to the size distribution.

particles on stage D and ~7.5% and ~3.8% of SRFA particles on stages D and E, respectively, larger than the 100% collection efficiency cut-off size of the previous stage particles, which might bounce from higher to lower stages.[89] The fraction of these bounced particles depends on the particles' properties, such as viscosity and density, and environmental conditions, such as relative humidity and temperature.[90] Moreover, the cut-off sizes of each stage are based on aerodynamic diameter, while the CCSEM-EDX measures the projected area equivalent diameter, which differs from the aerodynamic particle size.

3.3 Vertical gradient of aerosol properties using the STAC platform

Fig. 4 shows a representative example of a flight pattern during field deployment of the STAC platform at the ARM's TBS at the SGP site on February 14th, 2022, including the total particle concentration, temperature, RH, and altitude. Representative raw data from the OPC and microAeth are shown in Fig. S2,† indicating the variation of particle concentration and their light absorption properties at different altitudes. Insets in Fig. 4 show the combined size-resolved chemical composition obtained from CCSEM-EDX analysis of stage C and stage D samples for 5 STAC impactors (IM1–IM5) collected at about 200 m, 200–400 m, 400 m, 400–700 m, and 700–850 m AGL, respectively. Representative ESEM images of particles collected on each stage for IM5 (700–850 m) are shown in Fig. S3.† Overall, Fig. 4 shows variations in the ambient conditions, particle chemical composition, and particle concentrations at different altitudes. As expected, ambient temperature decreases and RH increases with increasing altitude. The CPC data show a higher concentration of particles at 200–400 m AGL and 700–850 m AGL altitude ranges than that of other samples collected at different altitudes. The particle size ranges from CCSEM-EDX analysis were not significantly different for samples at different altitudes. However, size distribution varies at different altitudes. For example, at a lower altitude (200 m AGL), the mode is shifted towards a larger size (~1 μm), while in the highest altitude range (700–850 m), the mode is towards smaller particles (~0.2 μm). Overall, these size ranges exceed the expected

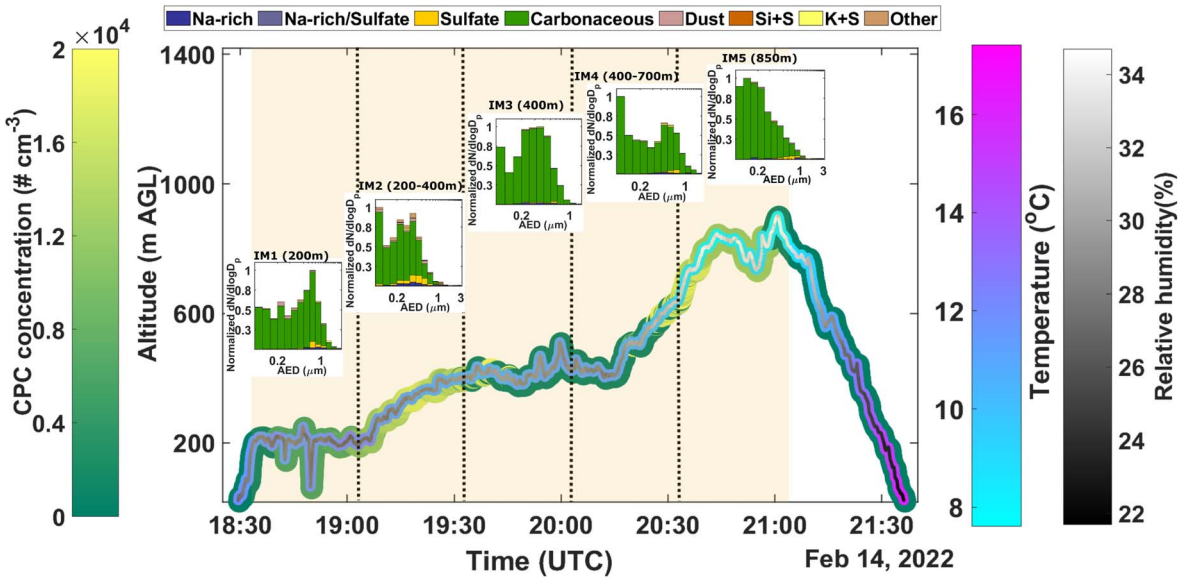

Fig. 4 TBS profile during one of the flights on February 14th, 2022, at the ARM SGP site. Ambient aerosol particle samples were collected using the STAC platform at about 200, 200–400, 400, 400–700, and 700–850 m AGL. The color bars on the left represent the total particle concentration of particles smaller than 1 μm retrieved from the CPC. The color bars on the right represent relative humidity and temperature. The figures in the insets show the combined size-resolved composition obtained from stage C and stage D samples for 5 STAC impactor samples collected at different AGL altitudes (IM1 (200 m), IM2 (200–400 m), IM3 (400 m), IM4 (400–700 m), and IM5 (700–850 m)) The shaded red area indicates the collection periods for 4-stage STAC impactors separated by the vertical black dashed lines. AED stands for area equivalent diameter.

collection size range of stages C and D of STAC impactors, and we did not see particle aggregation based on ESEM images (see Fig. S3†). One potential explanation is that these particles might be in a liquid state with low viscosity so that they spread out and deform to a flat shape when they impact the substrate.[55,91,92] Another explanation is that large particles could bounce from higher to lower stages.[89] Fig. 4 shows that most of the particles collected during this flight on stages C and D are carbonaceous (~79.8–96.2%). Even if the major fractions of particles are carbonaceous at different altitudes, the size modes of

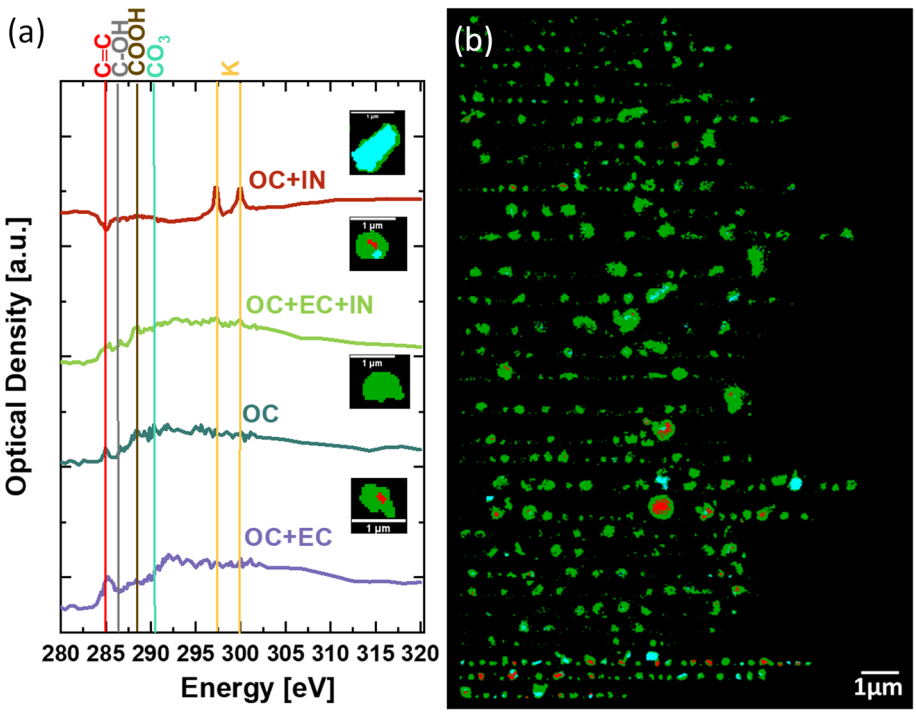

Fig. 5 (a) Representative carbon K-edge STXM-NEXAFS spectra of OC + IN, OC + EC + IN, OC, and OC + EC from different types of particles observed in IM1 (200 m) stage D. (b) STXM-NEXAFS was used to analyze the carbon speciation maps of all the particles from IM1 stage D. The different colors represent organic carbon (green), inorganics (cyan), and elemental carbon (red).

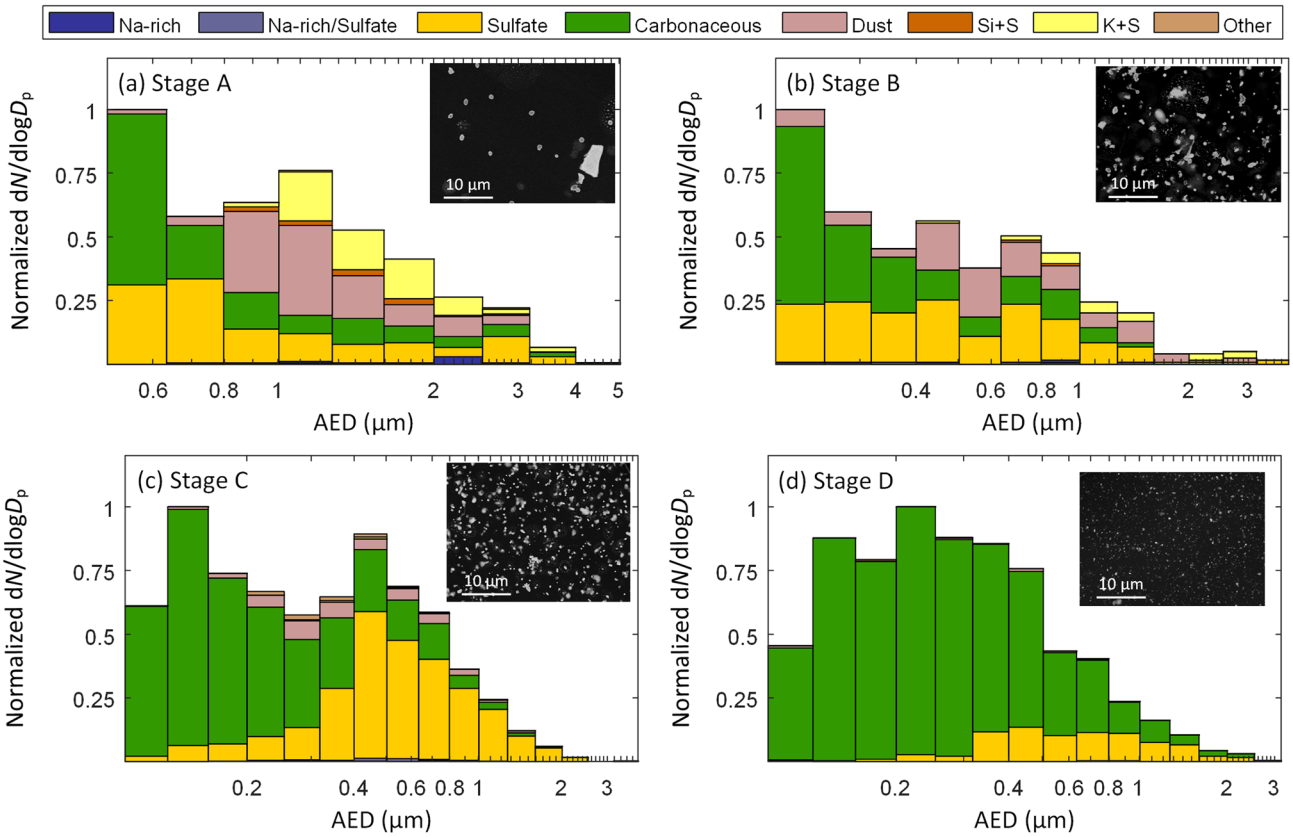

Fig. 6 CCSEM-EDX derived size-resolved chemical composition of ambient particles collected at the ARM SAIL ground site on December 9th, 2021, for (a) stage A, (b) stage B, (c) stage C, and (d) stage D. The insets are representative ESEM images of particles on each stage. AED stands for area equivalent diameter.

carbonaceous particles are different, suggesting different atmospheric processing along the vertical column. Moreover, from IM1 (200 m AGL) to IM2 (400 m AGL), the fraction of dust particles increased from ~2.8% to ~3.7%, and there was a significantly lower fraction of dust particles at 400 m, 400–700 m, and 700–850 m AGL (~0.4% and ~1.5%, respectively), indicating that the dust source might be local dust emission.[93] A small fraction of sulfate particles has been found in all samples (~1.0–7.0%), with the highest fraction at 200–400 m AGL (~7.0%). These sulfate particles in all samples have a size range between 0.2 and 1 μm. Sulfate particles larger than 0.6 μm might be products of cloud processing and subsequent transport back to low altitudes,[20,94–99] and those less than 0.6 μm might be generated from possible anthropogenic sources.[100,101]

Aerosol particle samples collected by using the STAC platform can be used for multi-modal analysis. For example, samples collected on TEM grids can be utilized for chemical imaging. Fig. 5 shows representative carbon K-edge STXM-NEXAFS spectra and chemical speciation maps of four typical particle mixing states we observed and the carbon speciation maps of all the particles analyzed by STXM-NEXAFS from STAC impactor stage D of IM1 (200 m). As shown in Fig. 5, IM1 is dominated by OC (~79.3%) at the time of sample collection. We also observed considerable fractions of IN (~9.0%) and EC (~8.4%) internally mixed and coated with OC, suggesting that our samples might have been aged during transport.[102–104]

We present another case study of size-resolved particle composition at the ground site to demonstrate the ability to collect a wide size range of ambient particles for 24 h using the STAC platform during the ARM Surface Atmosphere Integrated Field Laboratory (SAIL) ground site near Crested Butte, Colorado, on December 6th, 2021.[105] We show an example of size-resolved chemical composition using the same classification method[60] and a representative microscopy image of particles collected on stages A, B, C, and D (Fig. 6). Sample collection conditions are illustrated in Table S2.† As shown in Fig. 6, chemical compositions are highly variable across stage A to stage D. Carbonaceous particles dominate in all stages, and their number fractions increase from stage A (~29.2%) to stage D (~86.8%). Besides carbonaceous, sulfate particles are the second highest fraction in all stages (~10.9–43.7%). Dust and K + S particles have a high contribution in stages A and B (24.7% and 4.0% for stage A and 21.2% and 1.5% for stage B, respectively). These K + S particles are typically associated with aged biomass-burning aerosols.[106] The variance in SGP TBS samples and SAIL ground samples highlights the variations in aerosol composition at different geographical locations.

4. Conclusion

We present a vertical gradient of size-resolved aerosol composition using a newly developed lightweight automated size- and

time-resolved aerosol collector (STAC) platform integrated with environmental sensors. The system can be programmed to capture aerosols for different time intervals depending on the ambient aerosol concentrations. The platform has been deployed on the ARM's TBS in several ARM field campaigns. Our laboratory and field evaluation of the STAC platform suggests that it can be used to collect aerosol particles with broad size ranges with high time resolution (minutes to hours). For example, the system can collect particles while intersecting different layers of plumes or different layers of clouds to study the evolution of particles in the atmosphere. The vertical gradient of aerosol composition for the case study shows a similar composition of particles with a different size distribution, suggesting either different aerosol sources and/or atmospheric processing at different altitudes.

Simultaneous particle collections on various substrates facilitate multi-modal and correlative analysis to probe their physical (*e.g.*, the phase state and morphology), chemical (*e.g.*, the size-resolved chemical composition and mixing state), optical (light absorption and scattering), and ice nucleation properties. Besides sample collection, the STAC platform monitors meteorological conditions, aerosol particle size distribution, and optical properties. Thus, the STAC platform serves other atmospheric research, such as the vertical profile of aerosol chemical composition, multi-phase chemistry, and ice formation potential. The current limitation of the STAC platform includes the lack of information about sample loading on the substrate. Future studies will include data from controlled laboratory experiments with a range of particle concentrations monitored by the OPC with different sampling durations. The STAC software can be modified to convert the system into an adaptive and triggered sampling system to automatically switch the valve and move to the next sampling impactor once particle loading reaches a certain number using the integrated OPC particle concentration data. The system can be easily modified to be utilized as a long-term sample collection system at ground sites and remote locations. Furthermore, several other sensors for gas and volatile organic compound measurements can be integrated into the STAC platform for flux studies.

Data availability

The dataset used for this work has been deposited in zenodo, the open-access data repository under **https://doi.org/10.5281/zenodo.6915441**. The ARM data used in this study is available under the ARM data repository **https://www.arm.gov/data/**.

Author contributions

S. C. and Z. C. devised this project. Z. C., A. L., D. D., C. M. L., and S. C. designed the STAC platform. D. D. and C. M. L. operated the TBS and collected samples. A. L. designed the PCB board and developed the software for the STAC system. Z. C. performed the laboratory experiments and evaluated the performance of the STAC impactor. G. K. and F. M. supported the laboratory experiments. N. N. L. and Z. C. performed the CCSEM and STXM experiments and data analysis. N. N. L. performed sensor data analysis. Z. C. led the manuscript writing with inputs from other co-authors.

Conflicts of interest

The authors declare that they have no conflict of interest.

Acknowledgements

This research was performed on a project award (**https://10.46936/prtn.proj.2020.51252/60000164**) and used resources at the Environmental Molecular Sciences Laboratory (EMSL) and the Atmospheric Radiation Measurement facility (ARM), which are DOE Office of Science User Facilities. Both facilities are sponsored by the Biological and Environmental Research program and operated under Contract No. DE-AC05-76RL01830 (EMSL) and DE-FG03-00ER62913 and DE-FG03-97ER62338 (ARM). The ARM Program was sponsored by the U.S. Department of Energy, Office of Science, Office of Biological and Environmental Research, Climate and Environmental Sciences Division. We acknowledge the support staff at the SAIL site, especially Travis Guy and John Bilberry, and the ARM support staff for TBS operations. We thank Randolph Norheim and Hardeep Mehta for their support with the electronics component of the platform and James Ewing and the machine shop at PNNL for the fabrication of the platform. G. K. acknowledges support from the Atmospheric System Research (ASR) Program as part of the U.S. Department of Energy Office of Science's Biological and Environmental Research program. STXM-NEXAFS analysis at beamline 5.3.2 of the Advanced Light Source at the Lawrence Berkeley National Laboratory was supported by the Director, Office of Science, Office of Basic Energy Sciences of the U.S. Department of Energy under Contract No. DE-AC02-05CH11231.

References

1 G. Myhre, D. Shindell, F.-M. Bréon, W. Collins JF, J. Huang, D. Koch, *et al.*, *Climate Change 2013: the Physical Science Basis. Contribution of Working Group I to the Fifth Assessment Report of the Intergovernmental Panel on Climate Change, Chapter 8: Anthropogenic and Natural Radiative Forcing*, ed. T. F. Stocker, D. Qin, G.-K. Plattner, M. Tignor, S. K. Allen, J. Boschung, et al., Cambridge, United Kingdom and New York, NY, USA, 2013.

2 X. Luo, H. Bing, Z. Luo, Y. Wang and L. Jin, Impacts of atmospheric particulate matter pollution on environmental biogeochemistry of trace metals in soil-plant system: A review, *Environ. Pollut.*, 2019, **255**, 113138, DOI: **10.1016/j.envpol.2019.113138**, available from.

3 A. Laskin, J. Laskin and S. A. Nizkorodov, Chemistry of Atmospheric Brown Carbon, *Chem. Rev.*, 2015, **115**(10), 4335–4382, DOI: **10.1021/cr5006167**, available from:.

4 T. C. Bond, S. J. Doherty, D. W. Fahey, P. M. Forster, T. Berntsen, B. J. Deangelo, *et al.*, Bounding the role of black carbon in the climate system: A scientific

assessment, *J. Geophys. Res.: Atmos.*, 2013, **118**(11), 5380–5552.

5 H. Moosmüller, R. K. Chakrabarty and W. P. Arnott, Aerosol light absorption and its measurement: A review, *J. Quant. Spectrosc. Radiat. Transfer*, 2009, **110**(11), 844–878.

6 J. Fan, Y. Wang, D. Rosenfeld and X. Liu, Review of aerosol-cloud interactions: Mechanisms, significance, and challenges, *J. Atmos. Sci.*, 2016, **73**(11), 4221–4252.

7 N. Bellouin, J. Quaas, E. Gryspeerdt, S. Kinne, P. Stier, D. Watson-Parris, *et al.*, Bounding Global Aerosol Radiative Forcing of Climate Change, *Rev. Geophys.*, 2020, **58**(1), 1–45.

8 R. Saleh, From Measurements to Models: Toward Accurate Representation of Brown Carbon in Climate Calculations, *Curr. Pollut. Rep.*, 2020, 706.

9 M. Shiraiwa, K. Ueda, A. Pozzer, G. Lammel, C. J. Kampf, A. Fushimi, *et al.*, Aerosol Health Effects from Molecular to Global Scales, *Environ. Sci. Technol.*, 2017, **51**(23), 13545–13567.

10 S. S. Lim, T. Vos, A. D. Flaxman, G. Danaei, K. Shibuya, H. Adair-Rohani, *et al.*, A comparative risk assessment of burden of disease and injury attributable to 67 risk factors and risk factor clusters in 21 regions, 1990–2010: a systematic analysis for the Global Burden of Disease Study 2010, *Lancet*, 2012, **380**(9859), 2224–2260.

11 A. O. Lawal, L. M. Davids and J. L. Marnewick, Toxicology *in Vitro* Diesel exhaust particles and endothelial cells dysfunction : An update, *Toxicol. In Vitro*, 2016, **32**, 92–104, DOI: **10.1016/j.tiv.2015.12.015**, available from:.

12 M. Shrivastava, S. Lou, A. Zelenyuk, R. C. Easter, R. A. Corley, B. D. Thrall, *et al.*, Global long-range transport and lung cancer risk from polycyclic aromatic hydrocarbons shielded by coatings of organic aerosol, *Proc. Natl. Acad. Sci. U. S. A.*, 2017, **114**(6), 1246–1251.

13 K. Atwi, A. Mondal, J. Pant, Z. Cheng, O. El, I. Ijeli, *et al.*, Physicochemical properties and cytotoxicity of brown carbon produced under different combustion conditions, *Atmos. Environ.*, 2021, **244**, 117881, DOI: **10.1016/j.atmosenv.2020.117881**, Available from:.

14 W. Li, L. Shao, D. Zhang, C. U. Ro, M. Hu, X. Bi, *et al.*, A review of single aerosol particle studies in the atmosphere of East Asia: Morphology, mixing state, source, and heterogeneous reactions, *J. Cleaner Prod.*, 2016, **112**, 1330–1349, DOI: **10.1016/j.jclepro.2015.04.050**, available from.

15 A. P. Ault and J. L. Axson, Atmospheric Aerosol Chemistry: Spectroscopic and Microscopic Advances, *Anal. Chem.*, 2017, **89**(1), 430–452.

16 N. Riemer, A. P. Ault, M. West, R. L. Craig and J. H. Curtis, Aerosol Mixing State: Measurements, Modeling, and Impacts, *Rev. Geophys.*, 2019, **57**(2), 187–249.

17 L. Ferrero, G. Mocnik, B. S. Ferrini, M. G. Perrone, G. Sangiorgi and E. Bolzacchini, Vertical profiles of aerosol absorption coefficient from micro-Aethalometer data and Mie calculation over Milan, *Sci. Total Environ.*, 2011, **409**(14), 2824–2837, DOI: **10.1016/j.scitotenv.2011.04.022**, available from:.

18 L. Morawska, S. Thomas, D. Gilbert, C. Greenaway and E. Rijnders, A study of the horizontal and vertical profile of submicrometer particles in relation to a busy road, *Atmos. Environ.*, 1999, **33**(8), 1261–1274.

19 J. B. Renard, V. Michoud and J. Giacomoni, Vertical profiles of pollution particle concentrations in the boundary layer above paris (France) from the optical aerosol counter LOAC onboard a touristic balloon, *Sensors*, 2020, **20**(4), 1111.

20 B. Ervens, Modeling the Processing of Aerosol and Trace Gases in Clouds and Fogs, *Chem. Rev.*, 2015, **115**(10), 4157–4198.

21 Z. Li, J. Guo, A. Ding, H. Liao, J. Liu, Y. Sun, *et al.*, Aerosol and boundary-layer interactions and impact on air quality, *Natl. Sci. Rev.*, 2017, **4**(6), 810–833.

22 V. Ramanathan and Y. Feng, Air pollution, greenhouse gases and climate change: Global and regional perspectives, *Atmos. Environ.*, 2009, **43**(1), 37–50, DOI: **10.1016/j.atmosenv.2008.09.063**, available from:.

23 T. Su, Z. Li, C. Li, J. Li, W. Han, C. Shen, *et al.*, The significant impact of aerosol vertical structure on lower atmosphere stability and its critical role in aerosol-planetary boundary layer (PBL) interactions, *Atmos. Chem. Phys.*, 2020, **20**(6), 3713–3724.

24 Z. Kipling, P. Stier, J. P. Schwarz, A. E. Perring, J. R. Spackman, G. W. Mann, *et al.*, Constraints on aerosol processes in climate models from vertically-resolved aircraft observations of black carbon, *Atmos. Chem. Phys.*, 2013, **13**(12), 5969–5986.

25 Z. Kipling, P. Stier, C. E. Johnson, G. W. Mann, N. Bellouin, S. E. Bauer, *et al.*, What controls the vertical distribution of aerosol? Relationships between process sensitivity in HadGEM3-UKCA and inter-model variation from AeroCom Phase II, *Atmos. Chem. Phys.*, 2016, **16**(4), 2221–2241.

26 P. Forster, V. Ramaswamy, P. Artaxo, T. Berntsen, R. Betts, D. W. Fahey, *et al.*, Changes in Atmospheric Constituents and in Radiative Forcing, *Climate Change 2007: the Physical Science Basis Contribution of Working Group I to the Fourth Assessment Report of the Intergovernmental Panel on Climate Change*, Cambridge, United Kingdom and New York, NY, USA, 2007.

27 C. Textor, M. Schulz, S. Guibert, S. Kinne, Y. Balkanski, S. Bauer, *et al.*, Analysis and quantification of the diversities of aerosol life cycles within AeroCom, *Atmos. Chem. Phys.*, 2006, **6**(7), 1777–1813.

28 S. Kinne, M. Schulz, C. Textor, S. Guibert, Y. Balkanski, S. E. Bauer, *et al.*, An AeroCom initial assessment – Optical properties in aerosol component modules of global models, *Atmos. Chem. Phys.*, 2006, **6**(7), 1815–1834.

29 D. Bhattu, S. N. Tripathi and A. Chakraborty, Deriving aerosol hygroscopic mixing state from size-resolved CCN activity and HR-ToF-AMS measurements, *Atmos. Environ.*, 2016, **142**, 57–70.

30 J. Z. Khan, L. Sun, Y. Tian, Q. Dai, T. Hu and Y. Feng, Size Distribution of Ambient Particulate Matter and Its Constituent Chemical Species Involving Saccharides

During Early Summer in a Chinese Megacity, *Front. Environ. Sci.*, 2021, **9**, 1–15.

31 T. A. Pakkanen, K. Loukkola, C. H. Korhonen, M. Aurela, T. Mäkelä, R. E. Hillamo, *et al.*, Sources and chemical composition of atmospheric fine and coarse particles in the Helsinki area, *Atmos. Environ.*, 2001, **35**(32), 5381–5391.

32 W. Tefera, A. Kumie, K. Berhane, F. Gilliland, A. Lai, P. Sricharoenvech, *et al.*, Chemical characterization and seasonality of ambient particles (PM2.5) in the city centre of addis ababa, *Int. J. Environ. Res. Public Health*, 2020, **17**(19), 1–16.

33 J. D. Fast, L. K. Berg, L. Alexander, D. Bell, E. D'Ambro, J. Hubbe, *et al.*, Overview of the HI-SCALE Field Campaign: A New Perspective on Shallow Convective Clouds, *Bull. Am. Meteorol. Soc.*, 2019, **100**(5), 821–840.

34 Y. Kondo, H. Matsui, N. Moteki, L. Sahu, N. Takegawa, M. Kajino, *et al.*, Emissions of black carbon, organic, and inorganic aerosols from biomass burning in North America and Asia in 2008, *J. Geophys. Res.*, 2011, **116**(8), D08204.

35 A. J. Sedlacek, P. R. Buseck, K. Adachi, T. B. Onasch, S. R. Springston and L. Kleinman, Formation and evolution of tar balls from northwestern US wildfires, *Atmos. Chem. Phys.*, 2018, **18**(15), 11289–11301.

36 M. Val Martin, R. E. Honrath, R. C. Owen and Q. B. Li, Seasonal variation of nitrogen oxides in the central North Atlantic lower free troposphere, *J. Geophys. Res.*, 2008, **113**(17), 1–15.

37 J. Wang, R. Wood, M. P. Jensen, J. Christine Chiu, Y. Liu, K. Lamer, *et al.*, Aerosol and Cloud Experiments in the Eastern North Atlantic (ACE-ENA), *Bull. Am. Meteorol. Soc.*, 2022, **103**(2), E619–E641.

38 S. K. Shin, M. Tesche, Y. Noh and D. Müller, Aerosol-type classification based on AERONET version 3 inversion products, *Atmos. Meas. Tech.*, 2019, **12**(7), 3789–3803.

39 T. Evgenieva, L. Gurdev, E. Toncheva and T. Dreischuh, Optical and Microphysical Properties of the Aerosol Field over Sofia, Bulgaria, Based onAERONET Sun-PhotometerMeasurements, *Atmosphere*, 2022, **13**, 884, DOI: **10.3390/atmos13060884**.

40 L. Ferrero, D. Cappelletti, B. Moroni, G. Sangiorgi, M. G. Perrone, S. Crocchianti, *et al.*, Wintertime aerosol dynamics and chemical composition across the mixing layer over basin valleys, *Atmos. Environ.*, 2012, **56**, 143–153, DOI: **10.1016/j.atmosenv.2012.03.071**, available from:.

41 A. Maletto, I. G. McKendry and K. B. Strawbridge, Profiles of particulate matter size distributions using a balloon-borne lightweight aerosol spectrometer in the planetary boundary layer, *Atmos. Environ.*, 2003, **37**(5), 661–670.

42 I. G. McKendry, A. P. Sturman and J. Vergeiner, Vertical profiles of particulate matter size distributions during winter domestic burning in Christchurch, New Zealand, *Atmos. Environ.*, 2004, **38**(29), 4805–4813.

43 J. Li, Q. Fu, J. Huo, D. Wang, W. Yang, Q. Bian, *et al.*, Tethered balloon-based black carbon profiles within the lower troposphere of Shanghai in the 2013 East China smog, *Atmos. Environ.*, 2015, **123**, 327–338, DOI: **10.1016/j.atmosenv.2015.08.096**, available from:.

44 U. Egerer, M. Gottschalk, H. Siebert, A. Ehrlich and M. Wendisch, The new BELUGA setup for collocated turbulence and radiation measurements using a tethered balloon: First applications in the cloudy Arctic boundary layer, *Atmos. Meas. Tech.*, 2019, **12**(7), 4019–4038.

45 R. P. Lawson, K. Stamnes, J. Stamnes, P. Zmarzly, J. Koskuliks, C. Roden, *et al.*, Deployment of a tethered-balloon system for microphysics and radiative measurements in mixed-phase clouds at Ny-Ålesund and South Pole, *J. Atmos. Ocean. Technol.*, 2011, **28**(5), 656–670.

46 D. Dexheimer, M. Airey, E. Roesler, C. Longbottom, K. Nicoll, S. Kneifel, *et al.*, Evaluation of ARM tethered-balloon system instrumentation for supercooled liquid water and distributed temperature sensing in mixed-phase Arctic clouds, *Atmos. Meas. Tech.*, 2019, **12**(12), 6845–6864.

47 S. China, D. Dexheimer, N. N. Lata, A. S. M. Shawon, F. Mei, Z. Cheng, *et al.*, *Size and Time-Resolved Automated Aerosol Sampling Field Campaign Report*, 2021, available from:**https://www.arm.gov/publications/programdocs/doe-sc-arm-21-017.pdf**.

48 J. M. Creamean, G. De Boer, H. Telg, F. Mei, D. Dexheimer, M. D. Shupe, *et al.*, Assessing the vertical structure of Arctic aerosols using balloon-borne measurements, *Atmos. Chem. Phys.*, 2021, **21**(3), 1737–1757.

49 V. A. Marple, K. L. Rubow and S. M. Behm, A microorifice uniform deposit impactor (moudi): Description, calibration, and use, *Aerosol Sci. Technol.*, 1991, **14**(4), 434–436.

50 P. Demokritou, T. Gupta, S. Ferguson and P. Koutrakis, Development and Laboratory Performance Evaluation of a Personal Cascade Impactor, *J. Air Waste Manage. Assoc.*, 2002, **52**(10), 1230–1237.

51 M. Singh, C. Misra and C. Sioutas, Field evaluation of a personal cascade impactor sampler (PCIS), *Atmos. Environ.*, 2003, **37**(34), 4781–4793.

52 O. G. Raabe, D. A. Braaten, R. L. Axelbaum, S. V. Teague and T. A. Cahill, Calibration studies of the drum impactor, *J. Aerosol Sci.*, 1988, **19**(2), 183–195.

53 Y. Zhao, S. S. Cliff, A. S. Wexler, W. Javed, K. Perry, Y. Pan, *et al.*, Measurements of size- and time-resolved elemental concentrations at a California dairy farm, *Atmos. Environ.*, 2014, **94**, 773–781, DOI: **10.1016/j.atmosenv.2014.06.011**, Available from:.

54 M. A. Venecek, Y. Zhao, J. Mojica, C. E. McDade, P. G. Green, M. J. Kleeman, *et al.*, Characterization of the 8-stage Rotating Drum Impactor under low concentration conditions, *J. Aerosol Sci.*, 2016, **100**, 140–154, DOI: **10.1016/j.jaerosci.2016.07.007**, Available from:.

55 Z. Cheng, N. Sharma, K.-P. Tseng, L. Kovarik and S. China, Direct observation and assessment of phase states of ambient and lab-generated sub-micron particles upon humidification, *RSC Adv.*, 2021, **11**, 15264–15272.

56 M. A. Freedman, Liquid-Liquid Phase Separation in Supermicrometer and Submicrometer Aerosol Particles, *Acc. Chem. Res.*, 2020, **53**(6), 1102–1110.
57 S. China, C. Mazzoleni, K. Gorkowski, A. C. Aiken and M. K. Dubey, Morphology and mixing state of individual freshly emitted wildfire carbonaceous particles, *Nat. Commun.*, 2013, **4**, 2122.
58 J. Ching, K. Adachi, Y. Zaizen, Y. Igarashi and M. Kajino, Aerosol mixing state revealed by transmission electron microscopy pertaining to cloud formation and human airway deposition, *npj Clim. Atmos. Sci.*, 2019, **2**(1), 1–7, DOI: **10.1038/s41612-019-0081-9**, available from:.
59 K. Adachi, N. Oshima, Z. Gong, S. De Sá, A. P. Bateman, S. T. Martin, *et al.*, Mixing states of Amazon basin aerosol particles transported over long distances using transmission electron microscopy, *Atmos. Chem. Phys.*, 2020, **20**(20), 11923–11939.
60 N. N. Lata, B. Zhang, S. Schum, L. Mazzoleni, R. Brimberry, M. A. Marcus, *et al.*, Aerosol Composition, Mixing State, and Phase State of Free Tropospheric Particles and Their Role in Ice Cloud Formation, *ACS Earth Space Chem.*, 2021, **5**(12), 3499–3510.
61 S. China, B. Wang, J. Weis, L. Rizzo, J. Brito, G. G. Cirino, *et al.*, Rupturing of biological spores as a source of secondary particles in Amazonia, *Environ. Sci. Technol.*, 2016, **50**(22), 12179–12186.
62 E. J. Freney, K. Adachi and P. R. Buseck, Internally mixed atmospheric aerosol particles: Hygroscopic growth and light scattering, *J. Geophys. Res.*, 2010, **115**(19), 1–8.
63 D. A. Knopf, J. C. Charnawskas, P. Wang, B. Wong, J. M. Tomlin, K. A. Jankowski, *et al.*, Micro-spectroscopic and freezing characterization of ice-nucleating particles collected in the marine boundary layer in the eastern North Atlantic, *Atmos. Chem. Phys.*, 2022, **22**(8), 5377–5398.
64 D. P. Veghte, S. China, J. Weis, L. Kovarik, M. K. Gilles and A. Laskin, Optical Properties of Airborne Soil Organic Particles, *ACS Earth Space Chem.*, 2017, **1**(8), 511–521.
65 V. A. Marple and K. Willeke, *Fine Particles: Aerosol Generation, Measurement, Sampling, and Analysis*, ed. B. Y. H. LIU, Academic Press, Minneapolis, 1st edn, 1975.
66 Z. Cheng, K. Atwi, T. Onyima and R. Saleh, Investigating the dependence of light-absorption properties of combustion carbonaceous aerosols on combustion conditions, *Aerosol Sci. Technol.*, 2019, **53**(4), 419–434, DOI: **10.1080/02786826.2019.1566593**, available from:.
67 E. S. Cross, J. G. Slowik, P. Davidovits, J. D. Allan, D. R. Worsnop, J. T. Jayne, *et al.*, Laboratory and ambient particle density determinations using light scattering in conjunction with aerosol mass spectrometry, *Aerosol Sci. Technol.*, 2007, **41**(4), 343–359.
68 J. L. Hand and S. M. Kreidenweis, A New Method for Retrieving Particle Refractive Index and Effective Density from Aerosol Size Distribution Data, *Aerosol Sci. Technol.*, 2002, **36**(10), 1012–1026.
69 M. Hu, J. Peng, K. Sun, D. Yue, S. Guo, A. Wiedensohler, *et al.*, Estimation of size-resolved ambient particle density based on the measurement of aerosol number, mass, and chemical size distributions in the winter in Beijing, *Environ. Sci. Technol.*, 2012, **46**(18), 9941–9947.
70 Z. Li, Y. Wei, Y. Zhang, Y. Xie, L. Li, K. Li, *et al.*, Retrieval of Atmospheric Fine Particulate Density Based on Merging Particle Size Distribution Measurements: Multi-instrument Observation and Quality Control at Shouxian, *J. Geophys. Res.: Atmos.*, 2018, **123**(21), 12474–12488.
71 P. H. McMurry, X. Wang, K. Park and K. Ehara, The relationship between mass and mobility for atmospheric particles: A new technique for measuring particle density, *Aerosol Sci. Technol.*, 2002, **36**(2), 227–238.
72 L. Morawska, G. Johnson, Z. D. Ristovski and V. Agranovski, Relation between particle mass and number for submicrometer airborne particles, *Atmos. Environ.*, 1999, **33**(13), 1983–1990.
73 J. Rissler, E. Z. Nordin, A. C. Eriksson, P. T. Nilsson, M. Frosch, M. K. Sporre, *et al.*, Effective density and mixing state of aerosol particles in a near-traffic urban environment, *Environ. Sci. Technol.*, 2014, **48**(11), 6300–6308.
74 M. Pitz, J. Cyrys, E. Karg, A. Wiedensohler, H. E. Wichmann and J. Heinrich, Variability of apparent particle density of an urban aerosol, *Environ. Sci. Technol.*, 2003, **37**(19), 4336–4342.
75 W. C. Hinds, *Aerosol Technology Properties, Behavior, and Measurement of Airborne Particles*, WILEY-INTERSCIENCE: John Wiley & Sons, Inc., New York, 2nd edn, 1999.
76 P. Pokorná, N. Zíková, P. Vodička, R. Lhotka, S. Mbengue, A. Holubová Šmejkalová, *et al.*, Chemically speciated mass size distribution, particle density, shape and origin of non-refractory PM1measured at a rural background site in central Europe, *Atmos. Chem. Phys.*, 2022, **22**(9), 5829–5858.
77 Y. Zhou, N. Ma, Q. Wang, Z. Wang, C. Chen, J. Tao, *et al.*, Bimodal distribution of size-resolved particle effective density: Results from a short campaign in a rural environment over the North China Plain, *Atmos. Chem. Phys.*, 2022, **22**(3), 2029–2047.
78 P. Zieger, O. Väisänen, J. C. Corbin, D. G. Partridge, S. Bastelberger, M. Mousavi-Fard, *et al.*, Revising the hygroscopicity of inorganic sea salt particles, *Nat. Commun.*, 2017, **8**, 15883.
79 A. Laskin, T. W. Wietsma, B. J. Krueger and V. H. Grassian, Heterogeneous chemistry of individual mineral dust particles with nitric acid: A combined CCSEM/EDX, ESEM, and ICP-MS study, *J. Geophys. Res.*, 2005, **110**(10), D10208.
80 A. Laskin, J. P. Cowin and M. J. Iedema, Analysis of individual environmental particles using modern methods of electron microscopy and X-ray microanalysis, *J. Electron Spectrosc. Relat. Phenom.*, 2006, **150**(2–3), 260–274.
81 B. Wang and D. A. Knopf, Heterogeneous ice nucleation on particles composed of humic-like substances impacted by O3, *J. Geophys. Res.*, 2011, **116**(3), 1–14.
82 G. P. Schill, P. J. DeMott, E. J. T. Levin and S. M. Kreidenweis, Use of the Single Particle Soot Photometer (SP2) as a pre-filter for ice nucleation

measurements: effect of particle mixing state and determination of SP2 conditions to fully vaporize refractory black carbon, *Atmos. Meas. Tech.*, 2018, **11**(5), 3007–3020.

83 R. C. Moffet, A. V. Tivanski and M. K. Gilles, Scanning Transmission X-ray Microscopy: Applications in Atmospheric Aerosol Research, *Fundamentals and Applications in Aerosol Spectroscopy*, ed. R. Signorell and J. P. Reid, Taylor and Francis Books, Inc., Boca Raton, FL, 2011, pp. 419–462.

84 R. E. O'Brien, A. Neu, S. A. Epstein, A. C. Macmillan, B. Wang, S. T. Kelly, *et al.*, Physical properties of ambient and laboratory-generated secondary organic aerosol, *Geophys. Res. Lett.*, 2014, **41**, 4347–4353.

85 M. Fraund, T. Park, L. Yao, D. Bonanno, D. Q. Pham and R. C. Moffet, Quantitative capabilities of STXM to measure spatially resolved organic volume fractions of mixed organic/inorganic particles, *Atmos. Meas. Tech.*, 2019, **12**(3), 1619–1633.

86 J. M. Tomlin, K. A. Jankowski, F. A. Rivera-adorno, M. Fraund, B. H. Stirm, R. Kaeser, *et al.*, Chemical Imaging of Fine Mode Atmospheric Particles Collected from a Research Aircraft over Agricultural Fields, *ACS Earth Space Chem.*, 2020, **4**(11), 2171–2184.

87 R. C. Moffet, T. Henn, A. Laskin and M. K. Gilles, Automated chemical analysis of internally mixed aerosol particles using X-ray spectromicroscopy at the carbon K-edge, *Anal. Chem.*, 2010, **82**(19), 7906–7914.

88 D. Q. Pham, R. O'Brien, M. Fraund, D. Bonanno, O. Laskina, C. Beall, *et al.*, Biological Impacts on Carbon Speciation and Morphology of Sea Spray Aerosol, *ACS Earth Space Chem.*, 2017, **1**(9), 551–561.

89 Y. S. Cheng and H. C. Yeh, Particle Bounce in Cascade Impactors, *Atmos. Environ.*, 1979, **10**, 229–234.

90 J. P. Mitchell, M. W. Nagel, V. Avvakoumova, H. MacKay and R. Ali, The abbreviated impactor measurement (AIM) concept: Part 1 – Influence of particle bounce and re-entrainment – Evaluation with a "dry" pressurized metered dose inhaler (pMDI)-Based formulation, *AAPS PharmSciTech*, 2009, **10**(1), 243–251.

91 Z. Cheng, M. Morgenstern, B. Zhang, M. Fraund, N. N. Lata, M. A. Marcus, *et al.*, Particle phase-state variability in the North Atlantic free troposphere during summertime is determined by atmospheric transport patterns and sources, *Atmos. Chem. Phys.*, 2022, **22**, 9033–9057.

92 J. P. Reid, A. K. Bertram, D. O. Topping, A. Laskin, S. T. Martin, M. D. Petters, *et al.*, The viscosity of atmospherically relevant organic particles, *Nat. Commun.*, 2018, **9**, 956.

93 H. Yu, L. A. Remer, M. Chin, H. Bian, R. G. Kleidman and T. Diehl, A satellite-based assessment of transpacific transport of pollution aerosol, *J. Geophys. Res.*, 2008, **113**(D14), 1–15.

94 B. Ervens, A. Sorooshian, A. M. Aldhaif, T. Shingler, E. Crosbie, L. Ziemba, *et al.*, Is there an aerosol signature of chemical cloud processing?, *Atmos. Chem. Phys.*, 2018, **18**(21), 16099–16119.

95 A. K. Y. Lee, P. Herckes, W. R. Leaitch, A. M. MacDonald and J. P. D. Abbatt, Aqueous OH oxidation of ambient organic aerosol and cloud water organics: Formation of highly oxidized products, *Geophys. Res. Lett.*, 2011, **38**(11), 2–6.

96 B. Ervens, B. J. Turpin and R. J. Weber, Secondary organic aerosol formation in cloud droplets and aqueous particles (aqSOA): A review of laboratory, field and model studies, *Atmos. Chem. Phys.*, 2011, **11**(21), 11069–11102.

97 S. Zhou, S. Collier, D. A. Jaffe and Q. Zhang, Free Tropospheric Aerosols at the Mt. Bachelor Observatory: More Oxidized and Higher Sulfate Content Compared to Boundary Layer Aerosols, *Atmos. Chem. Phys.*, 2019, **19**, 1571–1585.

98 H. Kim, S. Collier, X. Ge, J. Xu, Y. Sun, W. Jiang, *et al.*, Chemical processing of water-soluble species and formation of secondary organic aerosol in fogs, *Atmos. Environ.*, 2019, **200**, 158–166, DOI: **10.1016/j.atmosenv.2018.11.062**, available from:.

99 A. K. Y. Lee, K. L. Hayden, P. Herckes, W. R. Leaitch, J. Liggio, A. M. MacDonald, *et al.*, Characterization of aerosol and cloud water at a mountain site during WACS 2010: Secondary organic aerosol formation through oxidative cloud processing, *Atmos. Chem. Phys.*, 2012, **12**(15), 7103–7116.

100 A. Sorooshian, M. L. Lu, F. J. Brechtel, H. Jonsson, G. Feingold, R. C. Flagan, *et al.*, On the source of organic acid aerosol layers above clouds, *Environ. Sci. Technol.*, 2007, **41**(13), 4647–4654.

101 J. Z. Yu, X. F. Huang, J. Xu and M. Hu, When aerosol sulfate goes up, so does oxalate: Implication for the formation mechanisms of oxalate, *Environ. Sci. Technol.*, 2005, **39**(1), 128–133.

102 S. China, B. Scarnato, R. C. Owen, B. Zhang, M. T. Ampadu, S. Kumar, *et al.*, Morphology and mixing state of aged soot particles at a remote marine free troposphere site: Implications for optical properties, *Geophys. Res. Lett.*, 2015, **42**(4), 1243–1250.

103 G. Motos, J. C. Corbin, J. Schmale, R. L. Modini, M. Bertò, P. Kupiszewski, *et al.*, Black Carbon Aerosols in the Lower Free Troposphere are Heavily Coated in Summer but Largely Uncoated in Winter at Jungfraujoch in the Swiss Alps, *Geophys. Res. Lett.*, 2020, **47**(14), 1–10.

104 W. Li, J. Sun, L. Xu, Z. Shi, N. Riemer, Y. Sun, *et al.*, A conceptual framework for mixing structures in individual aerosol particles, *J. Geophys. Res.: Atmos.*, 2016, **121**(22), 784–798.

105 D. Feldman, A. Aiken, W. Boos, R. Carroll, V. Chandrasekar, W. Collins, *et al.*, *Surface Atmosphere Integrated Field Laboratory (SAIL) Science Plan*, 2021.

106 J. E. Pachon, R. J. Weber, X. Zhang, J. A. Mulholland, A. G. Russell and J. E. Pachon, Revising the use of potassium (K) in the source apportionment of PM2.5, *Atmos. Pollut. Res.*, 2013, **4**(1), 14–21, DOI: **10.5094/APR.2013.002**, available from:.

